NANO LETTERS

pubs.acs.org/NanoLett Letter

Advanced Quantitative Phase Microscopy Achieved with Spatial Multiplexing and a Metasurface

Junxiao Zhou,[†] Ang Li,[†] Ming Lei, Jie Hu, Guanghao Chen, Zachary Burns, Fanglin Tian, Xinyu Chen, Yu-Hwa Lo, Din Ping Tsai, and Zhaowei Liu*

Cite This: https://doi.org/10.1021/acs.nanolett.4c06039 Read Online

ACCESS | Metrics & More | Article Recommendations | Supporting Information

ABSTRACT: Quantitative optical phase information provides an alternative method to observe biomedical properties, where conventional phase imaging fails. Phase retrieval typically requires multiple intensity measurements and iterative computations to ensure uniqueness and robustness against detection noise. To increase the measurement speed, we propose a single-shot quantitative phase imaging method with metasurface optics that can be conveniently integrated into conventional imaging systems with minimal modification. The improvement of the measurement speed is simultaneously made possible by combining deep learning with the transport-of-intensity equation. As a proof-of-concept, we demonstrate phase retrieval on both calibrated phase objects and biological specimens by using an imaging system integrated with our metasurface. When combined with the matched neural network, the system yields result with errors as low as 5% and increased space-bandwidth-product. A multitude of commercial applications can benefit from the compactness and rapid implementation of our proposed method.

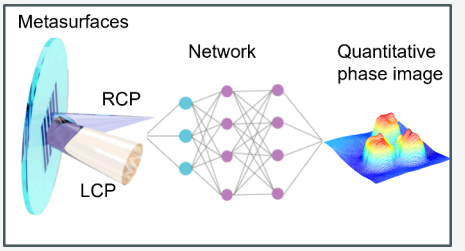

KEYWORDS: *Quantitative phase information, Metasurface, Deep learning, Transport-of-intensity equation*

Metasurfaces are praised for their capability in manipulating light at subwavelength scales and achieving arbitrary wavefront modulation.[1−4] Due to their low intrinsic loss, optical designers have long favored dielectric materials over plasmonic materials for metasurface design, potentially replacing traditional optical elements,[5] including refractive lenses,[6−8] beam manipulation element,[9−13] and optical analog computing devices,[14−21] such as edge detection, which has been used for observing the phase objects which lacks contrast and absorbs no light. In recent years, quantitative phase imaging (QPI) has garnered increasing attention with the emergence of multifunctional metasurfaces. QPI is a useful method to extract information more than the shape and size of the objects. Integrating functional metasurfaces in QPI applications has the potential to reduce the overall sizes and weights in conventional QPI systems and promote their widespread application beyond laboratory settings.[22−27] QPI methods based on interferometry often face limitations related to environmental stability and image resolution.[28] Consequently, direct phase retrieval based on transport-of-intensity (TIE) method has gained popularity in research.[29] It has been demonstrated the transitioning of intensity distribution along the wave propagation direction can provide the phase distribution of the object being imaged.[30] Therefore, TIE-QPI requires at least two intensity measurements offset from the ideal focal plane.[31] Since traditional refractive and diffractive optical elements are incapable of generating multiple copies of the image with solely controlled focal depths and offsets, typical TIE-QPI setups acquire the intensity measurements by mechanically displacing the image plane along the propagation direction of images and suffer low detection speed. We can rid ourselves of this inconvenience by redesigning the imaging setup with metasurface optics.

Another major speed improvement can be made by changing the phase retrieval process. After the intensity measurement, a reconstruction pipeline attempts to recover the phase of the scattered field and its associated properties of the object. Aside from the lengthy iterative computation, conventional reconstruction algorithms such as Fast Fourier Transform (FFT)-TIE, Discrete Fourier Transform DCT-TIE are susceptible to image boundaries, noise, or low-frequency artifacts. These algorithms require empirical knowledge of hyperparameters, and certain approximations of the objects being imaged must be assumed to ensure uniqueness and robustness of solutions. In recent years, computational imaging has again attracted numerous attentions due to the rapid development of high-performance computing and the increasingly user-friendly machine-learning framworks.[32−44] Physics-informed neural networks, as a branch of artificial neural

Received: November 27, 2024
Revised: January 17, 2025
Accepted: January 17, 2025

networks, have found wide applications and excellent generalization performance in linear systems.[45,46] Based on these findings, it is possible that the iterative TIE for the QPI reconstruction pipeline can be transformed by physics-informed neural networks, which, once trained, can predict the phase information in the blink of an eye and with higher confidence in the solutions.

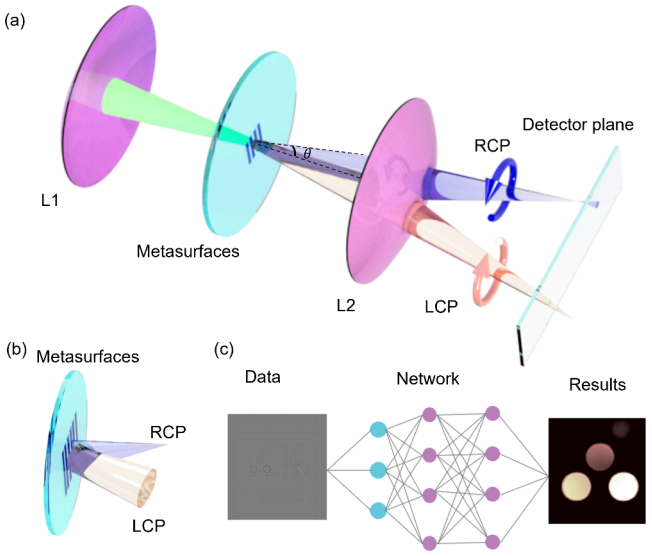

Figure 1. (a) TIE-QPI pipeline. In the 4*f* system, the RCP component is focused before the detector plane and LCP is defocused after the detector plane. (b) The metasurface's ability to diverge left-circularly polarized (LCP) and converge right-circularly polarized (RCP) light, directing them in divergent directions. (c) The captured CCD image, containing both far-sighted and near-sighted intensity images, are processed using deep learning techniques for quantitative phase reconstruction.

In the following sections of this work, we first introduce the design of a functional metasurface and a matching surrogate neural network for TIE, along with the integration of these two components into a general imaging setup for snapshot phase retrieval. When inserted in an imaging setup, the metasurface simultaneously splits the original image into two copies with opposite polarizations. This results in two spin images with ultrasmall focal length differences along the optical axis, formed at different detector locations. This spatial separation enables the simultaneous capture of two slightly blurred images, eliminating the need for specimen or camera displacements. With the single-shot intensity measurement, a trained neural-network-based phase retrieval algorithm then reconstructs the phase information on the object. Such a configuration leads to a more stable setup, a faster acquisition system, and the potential for a rapid and necessary QPI configuration. The system presented here comprises a single metasurface and is fundamentally distinct, being noninterferometric and achieved in a single-shot manner.

Figure 1 illustrates a QPI pipeline with the proposed functional metasurface inserted into a generic imaging system. With the optimized phase function, the metasurface diverts the left-handed circular polarization (LCP) and right-handed circular polarization (RCP) images into separate directions and adds opposite focal power to the two polarizations such that the CCD is near-sighted for the RCP images and far-sighted for the LCP images, as shown in Figure 1(b). One configuration of particular interest is where the designed metasurface is positioned at the Fourier plane of the 4*f* system. Figure 1(a) shows a schematic diagram of the optical path principle of imaging, where the light illuminating the sample is imaged on the CCD after passing through the 4*f* system. Following image acquisition, deep learning aids in phase reconstruction, as presented in Figure 1(c).

When the metasurface is positioned at the Fourier plane, a linearly polarized beam is incident on the object; the first lens (L1) computes the Fourier transform of the electric field of the incident beam. The dielectric metasurfaces function by inducing opposite transverse and longitudinal phase shifts on the LCP and RCP components. Therefore, the phase spectrum of the metasurface can be expressed as follows:

$$\Phi_{\mathrm{LCP,RCP}}(u, v) = \sigma_{\pm} 2\pi u f \tan\theta + \sigma_{\pm} k[\sqrt{f_{\mathrm{MS}}^2 + (\lambda f u)^2 + (\lambda f v)^2} - f_{\mathrm{MS}}] \quad (1)$$

where λ is the working wavelength, f = 50 mm is the focal length of the lenses in the 4*f* system, and f_{MS} is set to 5 m. The value of tan θ is determined by the metasurface parameter $\tan\theta = \frac{\lambda}{\Lambda}$, where Λ is the period of the metasurface. u and v are the spatial coordinates at the Fourier plane. $\sigma_{\pm} = \pm 1$ indicates the LCP and RCP components. As described by eq 1, the metasurface phase profile is that of a blazed grating that angularly separates the two polarizations by an angle θ. The two beams are concurrently captured by a camera. Mathematically, the complex output field at the camera plane is delineated as

$$E_{\mathrm{LCP,RCP}}(x, y) = \mathcal{F}^{-1}\{\mathcal{F}[E_{\mathrm{in}}(x, y)] \times \exp[i\Phi_{\mathrm{LCP,RCP}}(u, v)]\} \quad (2)$$

where $\mathcal{F}$ and $\mathcal{F}^{-1}$ is the Fourier (inverse Fourier) operator and (x,y) are the spatial coordinates at the input and output planes. The intensity profile captured by the camera is expressed as

$$\left| E_{\mathrm{in}}(x, y) \otimes \{\delta(x + \sigma_{\pm} f\tan\theta, y) + \mathcal{F}\{\exp\{\sigma_{\pm}[\sqrt{f_{\mathrm{MS}}^2 + (\lambda f u)^2 + (\lambda f v)^2} - f_{\mathrm{MS}}]\}\}\}\right|^2 \quad (3)$$

The TIE is derived from the parabolic wave equation and establishes a connection between $\Psi(x,y)$ representing the input field and its axial intensity derivative,[47] given by $\frac{\partial I(x,y)}{\partial z} = -\frac{\lambda}{2\pi}\nabla_{\perp}\cdot[I(x, y)\nabla_{\perp}\Psi(x, y)]$. Here, the symbol $\nabla_{\perp} = \frac{\hat{x}\partial}{\partial x} + \frac{\hat{y}\partial}{\partial y}$ denotes the two-dimensional gradient operator operating across the transverse coordinates. The variable $I(x,y)$ signifies the intensity distribution in the chosen plane. To compute the intensity derivative $\frac{\partial I(x,y)}{\partial z}$, one can utilize the defocused intensity distributions along the optical axis: $\frac{I(x,y,z+\Delta z/2)}{\Delta z} - \frac{I(x,y,z-\Delta z/2)}{\Delta z}$, where $\frac{\Delta z}{2}$ denotes the axis defocus distance.

Figure 2 illustrates the details of the fabricated dielectric metasurface. A photograph of the fabricated sample and its measured phase distribution is shown in (a) and (c), respectively. Figure 2(c) provides a schematic representation of the optical axis distribution of the sample, where α indicates the orientation of the metasurface structure. Figure 2(d)

https://doi.org/10.1021/acs.nanolett.4c06039
Nano Lett. XXXX, XXX, XXX−XXX

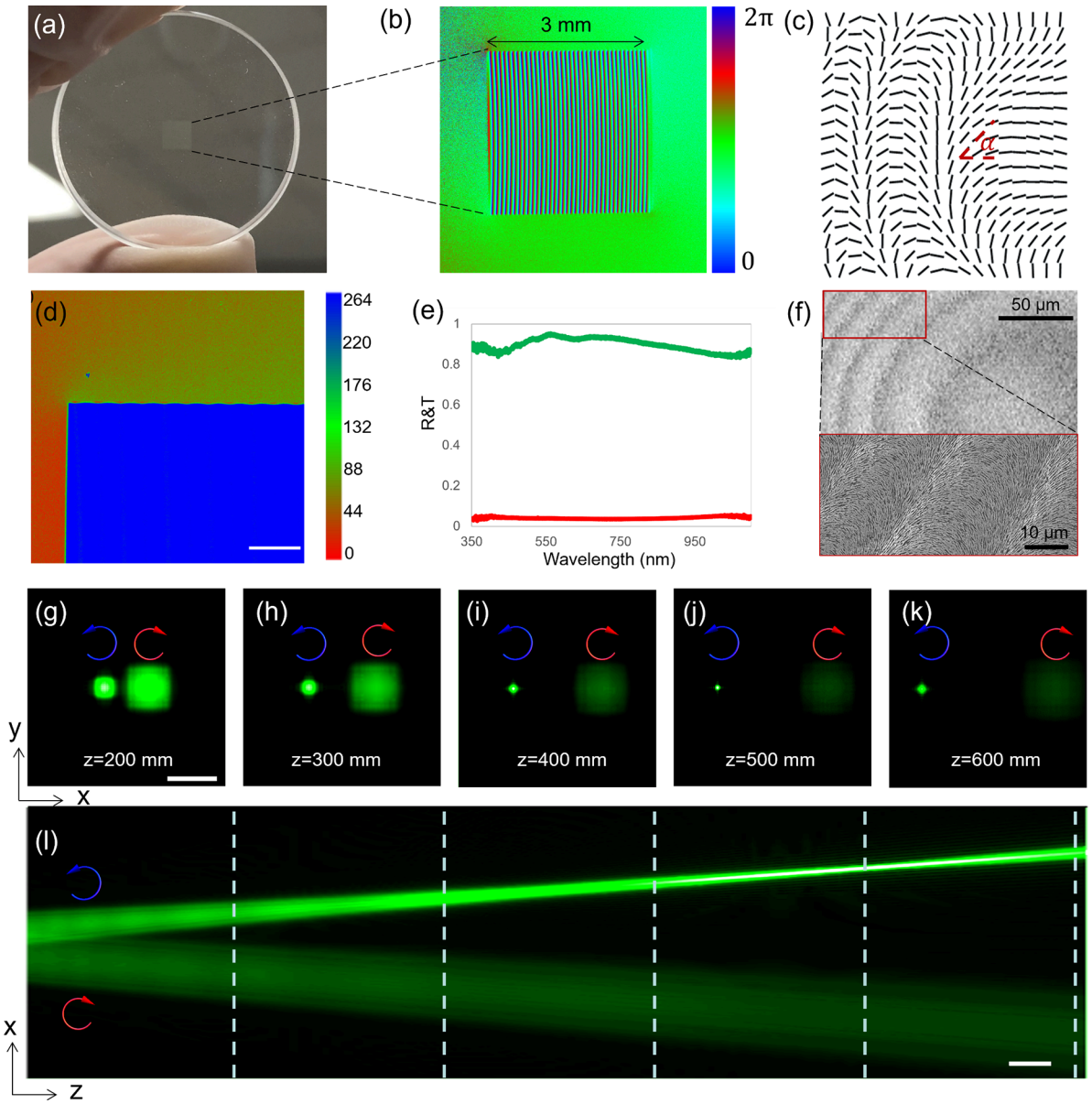

Figure 2. Characterization of the fabricated sample and the simulated intensity distribution of the metasurface. (a) The photograph of the metasurface and (b) birefringence image. (c) The schematic figure of the optical axis distribution. (d) The phase retardance image. Scale bar, 200 μm. (e) The wavelength-dependent transmission (T, green color) and reflection (R, red color). (f) The scanning electron microscope (SEM) images of the sample. Scale bar, 20 μm. Inset, zoomed in SEM image, scale bar 500 nm. (g-k) The intensity distribution along the *xy* plane at various propagation planes, as indicated by the dashed line in (l). Scale bar is 3 mm. (l) Simulated intensity distribution along the *xz* plane. Scale bar, 20 mm.

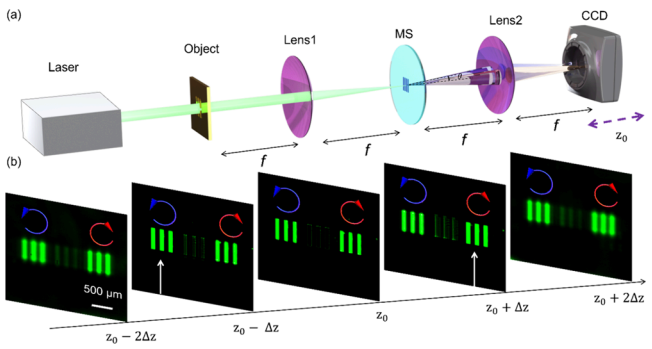

Figure 3. Experiment for metasurface function. (a) Experimental setup. (b) Intensity profile of the captured images.

presents the phase retardance image of the sample, indicating a phase retardance of 266 at a wavelength of 532 nm. Therefore, our sample can be considered a half-wave plate, capable of achieving higher circular polarization efficiency. The total transmission of the sample is around 95% at the working wavelength with a minimal reflection. The scanning electoral microscopy (SEM) images in Figure 2(f) depict the laser writing nanostructures. The sub-50 nm nanopores are helpful in reducing Rayleigh scattering and thereby enhance overall transmittance.[48,49] Details of the metasurface fabrication can be found in Note 1 in the Supporting Information.

To examine the functionality of the designed metasurface, simulated results are presented in Figure 2(g)-(l). The Fresnel diffraction of the modulated field is described by[50]

https://doi.org/10.1021/acs.nanolett.4c06039
Nano Lett. XXXX, XXX, XXX−XXX

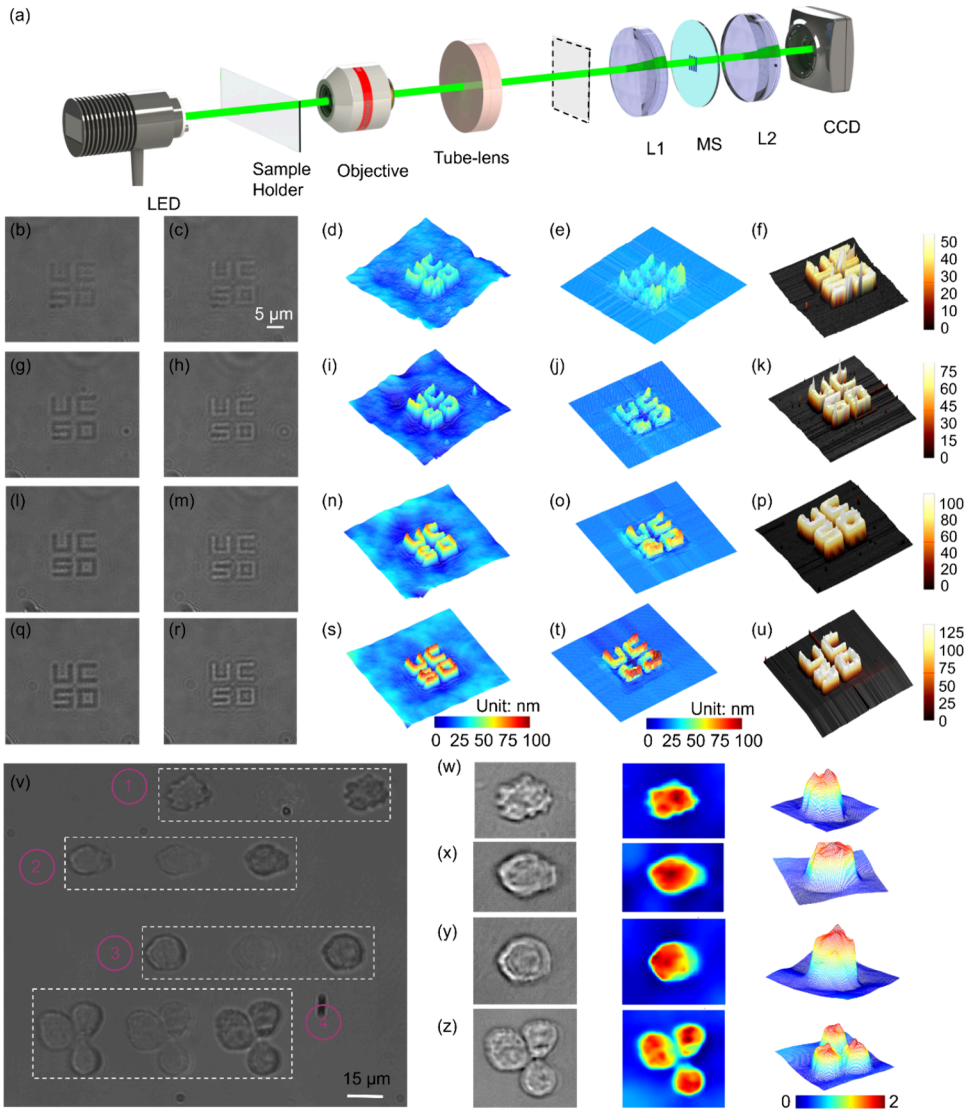

Figure 4. To test the proposed scheme, four different thicknesses with 50 nm (b-f), 75 nm (g-k), 100 nm (l-p), and 125 nm (q-u) as the phase objects are employed for our experiment. (b-u) The left two panels indicate the far-sighted and near-sighted images. The following panels are the extracted TIE-based QPI images, deep learning-assisted QPI images, and atomic force microscopy (AFM) images. The scale bar changes to 125 nm. (v-z) Experimental results for the deep learning assisted QPI for biomedical samples. (v) The raw images captured by CCD. The following three panels are the intensity difference of the far-sighted and a near-sighted images, the resulted QPI and the perceptive view of the QPI.

$$E_{\text{out}}^{u,v}(u,v) = \frac{\exp[ikz]}{i\lambda z}\iint A_0(x,y)\Phi_{\text{LCP,RCP}} \exp\left[\frac{ik}{2z}(u-x)^2 + (v-y)^2\right]dxdy \quad (4)$$

Here, $A_0(x,y) = e^{-x^2+y^2/\omega^2}$ represents an incident Gaussian distribution with a beam waist ω = 1 mm. $k = 2\pi/\lambda$, where λ denotes the wavelength of the light in a vacuum and z denotes the propagation distance. As observed from the simulation results, during propagation, the RCP light converges, while the LCP light continues to diverge as the light transmits to the metasurface, as evident from the *xy*-plane. Further validation of these findings is conducted in the *xz*-plane.

To verify the performance of the metasurface within the 4*f* optical system according to our design, the designed metasurface is positioned in the 4*f* optical setup and an amplitude mask is employed to access its properties (see Figure 3). The metasurface is situated at the Fourier plane of the imaging system. The object utilized is a custom-made amplitude mask (details can be found in the Supporting Information, Note 2). The CCD is moved from the image plane $z_0 - 2\Delta z$ to z_0 to $z_0 + 2\Delta z$. When the detector is distant from the focal plane, both the LCP and RCP components are blurred. At the $z_0 - \Delta z$ plane, the RCP component is focused. At the z_0 plane, both the RCP and the LCP components are slightly defocused. Hence, when the detector is positioned at the $z_0 + \Delta z$ plane, the LCP component is focused. When the detector is placed at $z_0 + 2\Delta z$, both components are defocused. Therefore, when the detector is at the z_0 plane, the intensities of LCP and RCP are slightly different, resulting in farsighted and nearsighted images, facilitating the use of the TIE.

Figure 4 illustrates the optical setup of an imaging system integrated with a conventional microscope system for the QPI. A beam from a green LED (Thorlabs, M530L4-C1) is collimated using a bandpass filter (528 nm ±1.4, Edmund Optics) for illumination. Microscopic samples are optically magnified using a microscope objective (0.6-NA, 40X,

https://doi.org/10.1021/acs.nanolett.4c06039
Nano Lett. XXXX, XXX, XXX−XXX

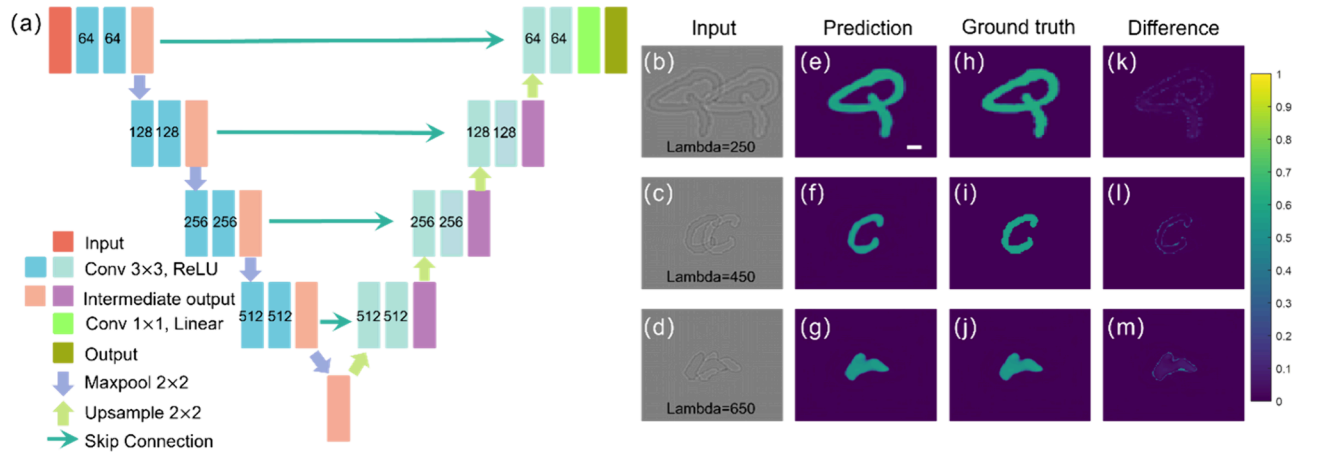

Figure 5. (a) Each block, as specified, contains a convolutional layer and an activation layer. The number on it represents the filter size. The 2D down sampling process is facilitated by Max Pooling layers, and the up-sampling process is carried out through interpolation. The skip connection is implemented by concatenating the outputs from the down-sampling and the upsampling processes at each level. Illustrates deep learning applied to inseparable data. (b-d) Depictions of 0the input. (e-g) The predicted QPI images. (h-j) The ground truth. (k-m) the difference between the prediction and the ground truth. The scale bar is 20 μm.

Olympus LUCPlanFLN) and tube lens (TTL 180-A, Thorlabs) to obtain a real intermediate image, as depicted within the gray dashed frame. The intermediate image is then aligned with the input of the following 4*f* system, as described in Figure 4. Both the near-sighted and the far-sighted images are captured simultaneously. It is observed that with thicker samples the contrast between the near-sighted and far-sighted images increases. To extract quantitative phase information, the TIE is employed.[51] The detailed phase object fabrication details and the reconstruction algorithm can be found in Supporting Information Notes 3 and 4.

In the reconstruction pipeline, a convolutional neural-network-based architecture known as ResNet is utilized. The constructed ResNet comprises 6 residual blocks for each filter size and accepts input images with one channel as LCP and the other as RCP. We used Adam Optimizer with the MSE loss function and an exponentially decayed learning rate, commencing at 1e-5 with a decay rate of 0.9 every 10 epochs, spanning a total of 150 epochs. The loss function is mean squared error (MSE):MSE $= \frac{1}{n}\sum_{i=1}^{n}(Y_i - \hat{Y}_i)^2$, where n is the number of data points, Y_i is the observed values, and $\hat{Y}_i$ is the predicated value. More details can be found in Note 5 in the Supporting Information. Comparing the reconstruction results obtained from the US-TIE and our approach to atomic force microscopy (AFM) measurement, consistency is generally observed, except for certain instances.

Furthermore, we test in situ QPI with our setup on lived HEK cells. These samples are cultured in a humidified incubator and 5% CO_2 in Dulbecco's modified Eagle's medium. Cells were incubated in a controlled environment of 37 at 37°C, 5% CO_2, and 70% humidity using a temperature and gas stage incubation system. Please refer to Supporting Information, Note 7, for cell preparation. Label-free imaging techniques in quantitative microscopy enable noninvasive examination of cells, offering deep insights into cell biology and medical research. This approach is instrumental in elucidating disease mechanisms, facilitating drug development, and advancing personalized medicine by providing intricate views of cellular structures and processes without relying on external markers. Results are illustrated in Figure 4(v)-(z).

The above-mentioned configuration generates two intensity measurements that are completely separated spatially on the sensor, at the cost of reduced field-of-view (FOV) and space-bandwidth-product. Here, we continue to propose the use of U-Net architecture to regain the FOV. This architecture achieves skip connection by propagating lost spatial information from the down sampling process to the feature-abundant up sampling process, accomplished by concatenating outputs within these two processes. Our U-Net consists of four down-sampling and up-sampling blocks, effectively transforming off-focused input intensity images through a down-sampling (encoder) and up-sampling (decoder) process into QPI output images. Adam optimizer with MSE loss function was used, involving a learning rate starting from 1e-6 and decaying exponentially with a decay rate of 0.9 every 10 epochs, over a total of 50 epochs, to carefully avoid overfitting. The training data set we generated for this task used random values such that the letters overlapped to different extents. Figure 5 illustrates deep learning applied to inseparable data. As observed, the difference between the prediction and the ground truth is less than 5%.

It should be noted that there is an important parameter during the metasurface design, one is the focus length, f_{MS}, which decides the intensity difference of the near- and far-sighted images. A large difference between them will contribute to inaccurate phase reconstruction due to the inaccurate estimation of the axial intensity derivation, as shown in Figure S6 in the Supporting Information. The accuracy of neural network reconstruction may be further enhanced by fine-tuning hyperparameters such as learning rates and exploring various regularization and optimization techniques. For predicting complex objects, the U-Net architecture can be expanded in depth or width and integrated with components, such as self-attention mechanisms. These mechanisms enable the network to focus on relevant features and relationships across spatial positions, thereby enhancing its ability to recover fine details from the overlapped LCP and RCP images.

In summary, we have introduced a noninterferometric TIE-based single-shot QPI approach by taking advantage of a functional metasurface and deep learning phase retrieval. This polarization-dependent metasurface enables the simultaneous

https://doi.org/10.1021/acs.nanolett.4c06039
Nano Lett. XXXX, XXX, XXX−XXX

capturing of two intensity measurements with different displacements along the propagation direction and eliminates the need for specimen or camera displacement in conventional QPI setups. The integration of a deep learning TIE phase retrieval pipeline also results in a fast and more robust phase reconstruction and further improves the detection speed of our QPI approach. We experimentally demonstrate phase retrievals on calibrated objects and biological specimens using the proposed approach, resulting in errors as low as 5%. In addition, the concept of extracting phase information from spatially overlapped intensity measurements is also discussed and demonstrated theoretically, potentially further increasing the space-bandwidth-product of our approach and making it suitable for ultrafast QPI imaging in a wide range of applications.

■ ASSOCIATED CONTENT

Supporting Information

The Supporting Information is available free of charge at https://pubs.acs.org/doi/10.1021/acs.nanolett.4c06039.

Metasurface sample fabrication; fabrication of the amplitude mask; fabrication of the UCSD phase mask; the principle of the reconstruction algorithm; deep learning network for phase reconstruction; training accuracy, loss reduction and convergence of the proposed deep-learning approach; cell preparation; simulation of the optical system; parameter analysis of the metasurface; effectiveness of U-Net architecture (PDF)

■ AUTHOR INFORMATION

Corresponding Author

Zhaowei Liu − *Department of Electrical and Computer Engineering, University of California, San Diego, La Jolla, California 92093, United States;* orcid.org/0000-0002-5732-8109; Email: zhaowei@ucsd.edu

Authors

Junxiao Zhou − *Department of Electrical and Computer Engineering, University of California, San Diego, La Jolla, California 92093, United States; Department of Electrical Engineering, City University of Hong Kong, Kowloon, Hong Kong 999077, China;* orcid.org/0000-0001-6168-8580

Ang Li − *Department of Electrical and Computer Engineering, University of California, San Diego, La Jolla, California 92093, United States*

Ming Lei − *Department of Electrical and Computer Engineering, University of California, San Diego, La Jolla, California 92093, United States;* orcid.org/0000-0001-6687-9044

Jie Hu − *Department of Electrical and Computer Engineering, University of California, San Diego, La Jolla, California 92093, United States*

Guanghao Chen − *Department of Electrical and Computer Engineering, University of California, San Diego, La Jolla, California 92093, United States*

Zachary Burns − *Department of Electrical and Computer Engineering, University of California, San Diego, La Jolla, California 92093, United States*

Fanglin Tian − *Department of Electrical and Computer Engineering, University of California, San Diego, La Jolla, California 92093, United States*

Xinyu Chen − *Department of Electrical and Computer Engineering, University of California, San Diego, La Jolla, California 92093, United States*

Yu-Hwa Lo − *Department of Electrical and Computer Engineering, University of California, San Diego, La Jolla, California 92093, United States*

Din Ping Tsai − *Department of Electrical Engineering, City University of Hong Kong, Kowloon, Hong Kong 999077, China;* orcid.org/0000-0002-0883-9906

Complete contact information is available at: https://pubs.acs.org/10.1021/acs.nanolett.4c06039

Author Contributions

†J.Z. and A.L. contributed equally to this work. J. Zhou proposed the idea. J. Zhou built the experimental setup and did the measurements. A. Li and Z. Burns did the neural network part. J. Zhou did simulation part and designed the metasurface sample. Jie Hu and F. Tian fabricated the artificial object and did the AFM measurement. M. Lei and G. Chen conducted the MS characterization. X. Chen grew the cell samples. J. Zhou and prepared all the figures. All the authors discussed the results and prepared the paper. Z. Liu supervised this work. All authors revised the manuscript.

Notes

The authors declare no competing financial interest.

■ ACKNOWLEDGMENTS

The generous partial support of this work by the Gordon and Betty Moore Foundation (to Z.L.). In addition, the author J. Zhou would like to thank Baobao Song for support and assistance.

■ REFERENCES

(1) Yu, N.; et al. Light propagation with phase discontinuities: generalized laws of reflection and refraction. *Science* **2011**, *334*, 333−337.

(2) Lin, D.; Fan, P.; Hasman, E.; Brongersma, M. L. Dielectric gradient metasurface optical elements. *Science* **2014**, *345*, 298−302.

(3) Cui, T. J.; et al. Roadmap on electromagnetic metamaterials and metasurfaces. *Journal of Physics: Photonics* **2024**, *6*, 032502.

(4) Jeon, D.; Shin, K.; Moon, S.-W.; Rho, J. Recent advancements of metalenses for functional imaging. *Nano Convergence* **2023**, *10*, 1−26.

(5) Yang, W.; Zhou, J.; Tsai, D. P.; Xiao, S. Advanced manufacturing of dielectric meta-devices. *Photonics Insights* **2024**, *3*, R04−R04.

(6) Wang, S.; et al. A broadband achromatic metalens in the visible. *Nat. Nanotechnol.* **2018**, *13*, 227−232.

(7) Zhou, J.; et al. Broadband photonic spin Hall meta-lens. *ACS Nano* **2018**, *12*, 82−88.

(8) Liu, Y.; Wu, Y.; Duan, R.; Fu, J.; Ovesen, M.; Lai, S. C. E.; Yeo, T.-E; Chee, J. Y.; Chen, Y.; Teo, S. L.; et al. Linear Electro-Optic Effect in 2D Ferroelectric for Electrically Tunable Metalens. *Adv. Mater.* **2024**, *36*, 2401838.

(9) Zhou, J.; Qian, H.; Luo, H.; Wen, S.; Liu, Z. A spin controlled wavefront shaping metasurface with low dispersion in visible frequencies. *Nanoscale* **2019**, *11*, 17111−17119.

(10) Zhou, J.; Zhang, W.; Liu, Y.; Ke, Y.; Liu, Y.; Luo, H.; Wen, S. Spin-dependent manipulating of vector beams by tailoring polarization. *Sci. Rep.* **2016**, *6*, 34276.

(11) Ahmed, H.; et al. Optical metasurfaces for generating and manipulating optical vortex beams. *Nanophotonics* **2022**, *11*, 941−956.

(12) Li, T.; Liao, K.; Zhou, H.; Geng, G.; Li, J.; Su, Z.; Wang, Y.; Hu, X.; Huang, L. On-Chip Metaline for Multiport Beam Splitting. *Adv. Opt. Mater.* **2023**, *11*, 2202527.

(13) Zhang, J. C.; Chen, M. K.; Fan, Y.; Chen, Q.; Chen, S.; Yao, J.; Liu, X.; Xiao, S.; Tsai, D. P. Miniature tunable Airy beam optical meta-device. *Opto-Electron. Adv.* **2024**, *7*, 230171.
(14) Zhou, J.; et al. Optical edge detection based on high-efficiency dielectric metasurface. *Proc. Natl. Acad. Sci. U.S.A.* **2019**, *116*, 11137−11140.
(15) Abdollahramezani, S.; Hemmatyar, O.; Adibi, A. Meta-optics for spatial optical analog computing. *Nanophotonics* **2020**, *9*, 4075−4095.
(16) Zhou, Y.; Zheng, H.; Kravchenko, I. I.; Valentine, J. Flat optics for image differentiation. *Nat. Photonics* **2020**, *14*, 316−323.
(17) Zangeneh-Nejad, F.; Sounas, D. L.; Alù, A.; Fleury, R. Analogue computing with metamaterials. *Nat. Rev. Mater.* **2021**, *6*, 207−225.
(18) Zhou, J.; Qian, H.; Zhao, J.; Tang, M.; Wu, Q.; Lei, M.; Luo, H.; Wen, S.; Chen, S.; Liu, Z. Two-dimensional optical spatial differentiation and high-contrast imaging. *Natl. Sci. Rev.* **2021**, *8*, nwaa176.
(19) Zhou, J.; Liu, S.; Qian, H.; Li, Y.; Luo, H.; Wen, S.; Zhou, Z.; Guo, G.; Shi, B.; Liu, Z. Metasurface enabled quantum edge detection. *Sci. Adv.* **2020**, *6*, No. eabc4385.
(20) Badloe, T.; et al. Bright-field and edge-enhanced imaging using an electrically tunable dual-mode metalens. *ACS Nano* **2023**, *17*, 14678−14685.
(21) Tang, P.; Li, X.; Kim, Y.; Xiao, L.; Wu, H.; Badloe, T.; Li, G.; Rho, J. Spin Hall effect of light in a Dichroic polarizer for multifunctional edge detection. *ACS Photonics* **2024**, *11*, 4170−4176.
(22) Kwon, H.; Arbabi, E.; Kamali, S. M.; Faraji-Dana, M.; Faraon, A. Single-shot quantitative phase gradient microscopy using a system of multifunctional metasurfaces. *Nat. Photonics* **2020**, *14*, 109−114.
(23) Zhou, J.; et al. Fourier Optical Spin Splitting Microscopy. *Phys. Rev. Lett.* **2022**, *129*, 020801.
(24) Wu, Q.; et al. Single-shot quantitative amplitude and phase imaging based on a pair of all-dielectric metasurfaces. *Optica* **2023**, *10*, 619−625.
(25) Li, L.; Wang, S.; Zhao, F.; Zhang, Y.; Wen, S.; Chai, H.; Gao, Y.; Wang, W.; Cao, L.; Yang, Y. Single-shot deterministic complex amplitude imaging with a single-layer metalens. *Sci. Adv.* **2024**, *10*, No. eadl0501.
(26) Engay, E.; Huo, D.; Malureanu, R.; Bunea, A.-I.; Lavrinenko, A. Polarization-Dependent All-Dielectric Metasurface for Single-Shot Quantitative Phase Imaging. *Nano Lett.* **2021**, *21*, 3820−3826.
(27) Zhou, H.; Li, X.; Ullah, N.; Geng, G.; Li, J.; Li, X.; Wang, Y.; Huang, L. Single-shot phase retrieval based on anisotropic metasurface. *Appl. Phys. Lett.* **2022**, *120*, 161702.
(28) Lee, K.; et al. Quantitative phase imaging techniques for the study of cell pathophysiology: from principles to applications. *Sensors* **2013**, *13*, 4170−4191.
(29) Streibl, N. Phase imaging by the transport equation of intensity. *Opt. Commun.* **1984**, *49*, 6−10.
(30) Nugent, K. A. The measurement of phase through the propagation of intensity: an introduction. *Contemp. Phys.* **2011**, *52*, 55−69.
(31) Wang, J.; Yu, R.; Ye, X.; Sun, J.; Li, J.; Huang, C.; Xiao, X.; Ji, J.; Shen, W.; Tie, Z.; et al. Quantitative phase imaging with a compact meta-microscope. *npj Nanophotonics* **2024**, *1*, 4.
(32) Burns, Z.; Liu, Z. Untrained, physics-informed neural networks for structured illumination microscopy. *Opt. Express* **2023**, *31*, 8714−8724.
(33) Lei, M.; et al. Super resolution label-free dark-field microscopy by deep learning. *Nanoscale* **2024**, *16*, 4703−4709.
(34) Chen, M. K.; Liu, X.; Sun, Y.; Tsai, D. P. Artificial intelligence in meta-optics. *Chem. Rev.* **2022**, *122*, 15356−15413.
(35) Kim, Y.; et al. Novel deep learning approach for practical applications of indentation. *Mater. Today Adv.* **2022**, *13*, 100207.
(36) Ma, W.; et al. Deep learning for the design of photonic structures. *Nat. Photonics* **2021**, *15*, 77−90.
(37) Xiong, B.; Xu, Y.; Li, W.; Ma, W.; Chu, T.; Liu, Y. Deep Learning Design for Multiwavelength Infrared Image Sensors Based on Dielectric Freeform Metasurface. *Adv. Opt. Mater.* **2024**, *12*, 2302200.
(38) Lee, S.; Kim, K.; Yang, Y.; Seong, J.; Jung, C.; Lee, H.-J.; Rho, J. Deep Learning-Driven Robust Glucose Sensing and Fruit Brix Estimation Using a Single Microwave Split Ring Resonator. *Laser Photonics Rev.* **2024**, *18*, 2300768.
(39) Rivenson, Y.; Zhang, Y.; Günaydın, H.; Teng, D.; Ozcan, A. Phase recovery and holographic image reconstruction using deep learning in neural networks. *Light Sci. Appl.* **2018**, *7*, 17141−17141.
(40) Badloe, T.; Yang, Y.; Lee, S.; Jeon, D.; Youn, J.; Kim, D. S.; Rho, J. Artificial Intelligence-Enhanced Metasurfaces for Instantaneous Measurements of Dispersive Refractive Index. *Adv. Sci.* **2024**, *11*, 2403143.
(41) Seo, J.; et al. Deep-learning-driven end-to-end metalens imaging. *Adv. Photonics* **2024**, *6*, 066002−066002.
(42) Wu, Q.; Xu, Y.; Zhao, J.; Liu, Y.; Liu, Z. Localized Plasmonic Structured Illumination Microscopy Using Hybrid Inverse Design. *Nano Lett.* **2024**, *24*, 11581−11589.
(43) Ma, W.; Xu, Y.; Xiong, B.; Deng, L.; Peng, R.-W.; Wang, M.; Liu, Y. Pushing the limits of functionality-multiplexing capability in metasurface design based on statistical machine learning. *Adv. Mater.* **2022**, *34*, 2110022.
(44) Lei, M.; et al. Deep Learning Assisted Plasmonic Dark-Field Microscopy for Super-Resolution Label-Free Imaging. *Nano Lett.* **2024**, *24*, 15724−15730.
(45) Cuomo, S.; Di Cola, V. S.; Giampaolo, F.; Rozza, G.; Raissi, M.; Piccialli, F.; et al. Scientific machine learning through physics−informed neural networks: Where we are and what's next. *Journal of Scientific Computing* **2022**, *92*, 88.
(46) Karniadakis, G. E.; et al. Physics-informed machine learning. *Nat. Rev. Phys.* **2021**, *3*, 422−440.
(47) Teague, M. R. Deterministic phase retrieval: a Green's function solution. *J. Opt. Soc. Am.* **1983**, *73*, 1434−1441.
(48) Lei, Y.; Shayeganrad, G.; Wang, H.; Sakakura, M.; Yu, Y.; Wang, L.; Kliukin, D.; Skuja, L.; Svirko, Y.; Kazansky, P. G.; et al. Efficient ultrafast laser writing with elliptical polarization. *Light Sci. Appl.* **2023**, *12*, 74.
(49) Sakakura, M.; Lei, Y.; Wang, L.; Yu, Y.-H.; Kazansky, P. G. Ultralow-loss geometric phase and polarization shaping by ultrafast laser writing in silica glass. *Light Sci. Appl.* **2020**, *9*, 1−10.
(50) Goodman, J. W. *Introduction to Fourier Optics*; Roberts and Company Publishers, 2005.
(51) Zhang, J.; Chen, Q.; Sun, J.; Tian, L.; Zuo, C. On a universal solution to the transport-of-intensity equation. *Opt. Lett.* **2020**, *45*, 3649−3652.

https://doi.org/10.1021/acs.nanolett.4c06039
Nano Lett. XXXX, XXX, XXX−XXX